Platinum(II) *N*-heterocyclic carbene complexes arrest metastatic tumor growth

Pui-Ki Wan[a,b], Ka-Chung Tong[a,b], Chun-Nam Lok[a,b], Chunlei Zhang[a,b], Xiao-Yong Chang[c], Kong-Hung Sze[d], Alice Sze Tsai Wong[e], and Chi-Ming Che[a,b,1]

[a]State Key Laboratory of Synthetic Chemistry, Department of Chemistry, The University of Hong Kong, Hong Kong, China; [b]Laboratory for Synthetic Chemistry and Chemical Biology, Hong Kong, China; [c]Department of Chemistry, Southern University of Science and Technology of China, Shenzhen, Guangdong 518055, China; [d]Department of Microbiology, The University of Hong Kong, Hong Kong, China; and [e]School of Biological Sciences, The University of Hong Kong, Hong Kong, China

Contributed by Chi-Ming Che, March 13, 2021 (sent for review December 17, 2020; reviewed by Angela Casini, Harry B. Gray, and Yi Lu)

Vimentin is a cytoskeletal intermediate filament protein that plays pivotal roles in tumor initiation, progression, and metastasis, and its overexpression in aggressive cancers predicted poor prognosis. Herein described is a highly effective antitumor and antimetastatic metal complex $[Pt^{II}(C^N^N)(NHC^{2Bu})]PF_6$ (Pt1a; HC^N^N = 6-phenyl-2,2′-bipyridine; NHC= *N*-heterocyclic carbene) that engages vimentin via noncovalent binding interactions with a distinct orthogonal structural scaffold. Pt1a displays vimentin-binding affinity with a dissociation constant of 1.06 μM from surface plasmon resonance measurements and fits into a pocket between the coiled coils of the rod domain of vimentin with multiple hydrophobic interactions. It engages vimentin in cellulo, disrupts vimentin cytoskeleton, reduces vimentin expression in tumors, suppresses xenograft growth and metastasis in different mouse models, and is well tolerated, attributable to biotransformation to less toxic and renal-clearable platinum(II) species. Our studies uncovered the practical therapeutic potential of platinum(II)–NHC complexes as effective targeted chemotherapy for combating metastatic and cisplatin-resistant cancers.

antimetastasis | metabolism | *N*-heterocyclic carbene | platinum | vimentin

Cancer invasion and metastasis are among the major causes of recurrence and mortality (1). Cancer metastasis begins with epithelial–mesenchymal transition (EMT), where epithelial cancer cells are transformed into mesenchymal cells equipped with motility, invasion, and stem cell-like properties (2–4). Vimentin (VIM), a canonical biomarker of EMT, is an intermediate filament protein playing pivotal roles in cytoskeletal architecture, organelle positioning, cell migration, and signaling; its overexpression in aggressive epithelial cancers of lung, breast, and prostate origin, and malignant melanoma, were reported to be associated with the acquisition of migratory and invasive phenotypes (5). The enhanced cell motility and invasiveness by VIM drive cancer cells' spreading from primary tumor to distant organs through the bloodstream or lymphatic system, resulting in a metastatic cascade (6, 7). Emerging evidence showed that high levels of VIM predicted a poor prognosis, particularly in patients with nonsmall cell lung cancer and triple-negative breast cancer (8–10). In view of its clinical significance, targeting VIM is an appealing strategy to combat advanced metastatic cancers that do not respond well to traditional chemotherapy or antihormonal therapy. Nevertheless, inhibitors/disruptors of VIM are scarce in the literature. Moreover, studies on the biomolecular interactions between VIM and its binding partner(s) are underdeveloped.

Several anticancer organic compounds have been reported to target VIM and display in vitro anticancer activities (11–14), but without mentioning their in vivo antimetastatic activity. Herein described are studies on the binding interaction of $[Pt^{II}(C^N^N)(NHC^{2Bu})]PF_6$ (**Pt1a**, where HC^N^N = 6-phenyl-2,2′-bipyridine and NHC = *N*-heterocyclic carbene) with VIM, and the associated anticancer properties. This complex has a scaffold with NHC ligand being orthogonal to the pincer $[Pt^{II}(C^N^N)]$ plane; such a unique structural scaffold renders **Pt1a** able to effectively bind to VIM noncovalently, in contrast to covalent modification by the majority of known VIM-targeting compounds. Our work features a rare example of an antitumor metal complex that engages VIM and shows promising in vivo antitumor activity in multiple mouse models bearing advanced metastatic tumors. This work also demonstrates an example of effective anticancer compound development by taking advantage of unique structural scaffolds of metal complexes for noncovalent interactions with an important molecular target of cancer as also revealed by recent work of Meggers, Che, Casini, and coworkers (15–20).

Results

Synthesis, Spectroscopic, and Self-Assembly Properties of Pincer Platinum(II) Complexes. The structures of the pincer Pt(II) complexes (**Pt1a–Pt6**) are depicted in Fig. 1. **Pt1a–Pt3** were reported previously (21, 22), while **Pt4–Pt6** are new complexes which were synthesized by refluxing cyclometalated Pt(II) precursors with imidazolium or benzimidazolium salts in acetonitrile and obtained as yellow or orange solids. In biological buffer solution and in the presence of glutathione, these Pt(II) complexes are stable for 72 h

Significance

Metastasis is a common cause of cancer mortality yet a daunting challenge in oncology. We have discovered a cytotoxic platinum(II) *N*-heterocyclic carbene complex that not only suppressed primary tumor growth in mice but also impeded metastatic growth of breast cancer and melanoma with long-term tolerance attributable to its eventual biotransformation into less-toxic, excretable products. It directly engages the cytoskeletal protein vimentin that plays pivotal roles in cancer stemness, survival, and invasion. It binds vimentin noncovalently via the distinct structural scaffold with a dissociation constant of 1 μM as determined by surface plasmon resonance, NMR, and molecular dynamics simulations, revealing the significance of harnessing noncovalent interactions of metal compounds with important molecular targets in the development of new anticancer metal medicines.

Author contributions: C.-M.C. designed research; P.-K.W., K.-C.T., C.Z., and X.-Y.C. performed research; K.-H.S. and A.S.T.W. contributed new reagents/analytic tools; P.-K.W., K.-C.T., C.-N.L., C.Z., and X.-Y.C. analyzed data; and P.-K.W., K.-C.T., C.-N.L., and C.Z. wrote the paper.

Reviewers: A.C., Technical University of Munich; H.B.G., California Institute of Technology; and Y.L., University of Illinois at Urbana–Champaign.

The authors declare no competing interest.

[1]To whom correspondence may be addressed. Email: cmche@hku.hk.

This article contains supporting information online at https://www.pnas.org/lookup/suppl/doi:10.1073/pnas.2025806118/-/DCSupplemental.

Published April 21, 2021.

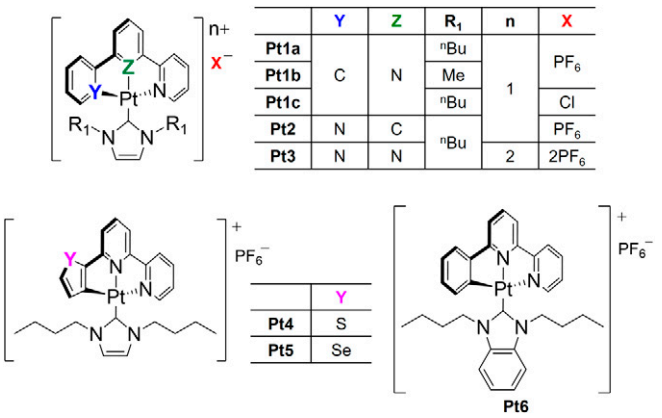

Fig. 1. Chemical structures of different pincer cyclometalated platinum(II) *N*-heterocyclic carbene complexes.

(*SI Appendix*, Figs. S1 and S2). As revealed by ultra-performance liquid chromatography/mass spectrometry (UPLC/MS) analysis, no new peak was found for **Pt1a** in culture medium for 72 h (*SI Appendix*, Fig. S3). The X-ray crystal structure of **Pt4** features a distorted planar molecular geometry with the NHC ligand at a dihedral angle of 68.5° to the [Pt^{II}(SC^N^N)] plane (Fig. 2*A* and *SI Appendix*, Tables S1–S3). The photophysical data of **Pt1a**–**Pt6** are summarized in *SI Appendix*, Figs. S4 and S5 and Table S4. The complexes display cyan to orange emission in degassed dichloromethane at 298 K with lifetimes (τ) of 0.5 to 10.0 μs and quantum yields of 0.8 to 36.3%. As revealed by transmission electron microscopy (TEM) images (Fig. 2*B* and *SI Appendix*, Fig. S6*A*), in aqueous solutions containing 1% CH_3CN the Pt(II)–NHC complexes (**Pt1a**–**Pt6**) self-assembled into spherical-like particles with diameters of 40 to 200 nm. From size distribution of nanoparticle tracking analysis (Fig. 2*C*), an average hydrodynamic diameter (D_h) of nanostructures formed by **Pt1a** was 128.1 ± 1.7 nm. The particle size of **Pt1b** bearing the *N*-methyl substituted NHC (D_h: 147.2 ± 1.2 nm) was larger than that of **Pt1a** with *N*-butyl chains. In RPMI 1640 culture medium containing 0.5% dimethyl sulfoxide (DMSO), **Pt1a** formed larger nanostructures with average D_h of 173.3 ± 3.1 nm (*SI Appendix*, Fig. S6*B*) compared with that formed in aqueous solution.

In Vitro Anticancer Properties and Metabolite Analysis. Previously we reported the low IC_{50} values (half-maximal inhibitory concentration) of the pincer platinum(II) complexes on cancer cell proliferation (21). In this work, a more extended list of cancerous cell lines of lung, breast, colorectal, and ovarian origin together with the noncancerous or cisplatin-resistant variant are included in antiproliferation assays as measured by naphthol blue-black staining (Table 1 and *SI Appendix*, Fig. S7) and validated by live/dead cell assays (calcein-AM/PI staining; *SI Appendix*, Figs. S8 and S9). Compared to cisplatin, the Pt(II) complexes (**Pt1a**–**Pt6**), except **Pt3**, exhibited higher anticancer activity with IC_{50} in a range of 0.03 to 1.49 μM. Particularly, **Pt1a** displayed a higher antiproliferative activity in NCI-H460 lung cancer cells compared to normal lung fibroblasts (CCD-19Lu) with around 30-fold difference in IC_{50} values. Changing the counteranion from PF_6^- as in **Pt1a** to Cl^- in **Pt1c** showed a negligible difference in cell growth inhibition. However, **Pt3**, being a dicationic charged complex, showed IC_{50} values higher by an order of magnitude in comparison to the monocationic analogs. **Pt1b** bearing two methyl groups was three- to fivefold less potent than **Pt1a** with two butyl chains for all the cancer cell lines examined. The Pt(II) complexes with either thiophene (**Pt4**) or selenophene (**Pt5**) on the C^N^N scaffold, benzimidazole-derived NHC ligand (**Pt6**), or N^C^N ligand (**Pt2**) displayed IC_{50} values comparable to that of **Pt1a**. It is worth noting that complexes (**Pt1a**–**Pt6**) displayed a comparable antiproliferation effect against both cisplatin-sensitive (A2780) and -resistant (A2780cis) ovarian cancer cell lines, whereas the potency of suppression for cisplatin was attenuated by 44-fold in IC_{50} on A2780cis compared to the parental cells.

The in vitro metabolism of **Pt1a**, **Pt2**, **Pt3**, and **Pt6** was studied with rat liver microsome using UPLC/MS analysis, which is detailed in *SI Appendix*. Compared to **Pt1a**, **Pt2** was shown to generate a similar number of metabolites. Dicationic **Pt3** displayed no observable biotransformation and **Pt6** containing benzimidazole-derived NHC ligand produced much less metabolites (*SI Appendix*, Fig. S10). The biotransformation of **Pt1a** to oxidized (**M1**–**M5**) and glucuronidated (**G1**–**G3**) platinum(II) species mainly involved the hydroxylation of the *N*-butyl chain of the coordinated NHC ligand (phase I reaction) and glucuronide conjugation to corresponding hydroxylated forms (phase II reaction) (*SI Appendix*, Figs. S11–S15). In vivo metabolism of **Pt1a** in a BALB/c mouse model revealed that oxidized species such as **M1** and **M2** were found as the principal monohydroxylated metabolites in the mouse urine after single-dose intravenous administration of **Pt1a** for 24 h (*SI Appendix*, Fig. S15*A*). On the other hand, dihydroxylated **M5** and glucuronidated (**G1** and **G3**) metabolites were also found in urine, in which **G1** was the major glucuronide species. These excreted metabolites can also be detected by UPLC/MS at 2 h after intravenous injection of **Pt1a** (*SI Appendix*, Fig. S15*B*). The proposed metabolites were synthesized independently, with chemical structures, IC_{50} values,

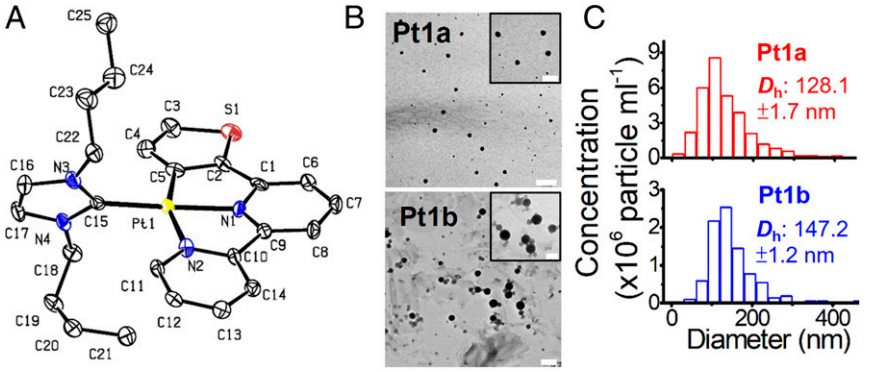

Fig. 2. (*A*) X-ray crystal structure of **Pt4** with omission of hydrogen atoms and counteranion. Thermal ellipsoids are shown at 50% probability level. (*B*) TEM images of self-assembled structures of **Pt1a** and **Pt1b** (1×10^{-4} M) in aqueous solution containing 1% CH_3CN. (Scale bar, 200 nm; *Inset*, 100 nm.) (*C*) Histograms of hydrodynamic diameters of particles formed by **Pt1a** and **Pt1b** in aqueous solution containing 1% CH_3CN.

Table 1. In vitro antiproliferative activity (IC_{50}; micromolar, 72 h) of Pt1a–Pt6 and cisplatin toward different human cancerous and normal cell lines

Complex	NCI-H460 (lung cancer)	MDA-MB-231 (breast cancer)	HCT116 (colorectal cancer)	A2780 (ovarian cancer)	A2780cis (ovarian cancer, cisplatin- resistant)	CCD-19Lu (lung fibroblast)
Pt1a	0.16 ± 0.01	0.20 ± 0.01	0.16 ± 0.01	0.06 ± 0.01	0.10 ± 0.01	4.74 ± 0.28
Pt1b	0.51 ± 0.06	1.06 ± 0.05	0.79 ± 0.08	0.21 ± 0.02	0.32 ± 0.01	9.52 ± 0.61
Pt1c	0.17 ± 0.01	0.26 ± 0.03	0.23 ± 0.03	0.14 ± 0.04	0.15 ± 0.06	5.18 ± 0.34
Pt2	0.31 ± 0.02	0.32 ± 0.05	0.30 ± 0.03	0.28 ± 0.02	0.32 ± 0.02	4.85 ± 0.51
Pt3	2.44 ± 0.34	3.26 ± 0.45	4.01 ± 0.35	9.83 ± 0.84	10.37 ± 0.84	>100
Pt4	0.18 ± 0.01	0.21 ± 0.02	0.16 ± 0.01	0.07 ± 0.01	0.10 ± 0.01	4.94 ± 0.32
Pt5	0.17 ± 0.01	0.21 ± 0.02	0.15 ± 0.01	0.05 ± 0.01	0.08 ± 0.01	4.81 ± 0.13
Pt6	0.13 ± 0.01	0.15 ± 0.01	0.11 ± 0.01	0.03 ± 0.002	0.06 ± 0.004	3.26 ± 0.17
Cisplatin	8.07 ± 0.80	10.24 ± 0.86	9.50 ± 0.05	0.32 ± 0.01	14.24 ± 0.95	38.21 ± 1.75

cellular uptake, and lipophilicity depicted in Fig. 3. The antiproliferative activity of the metabolites toward both cancer and normal cell lines are generally less effective than **Pt1a** (Fig. 3*B* and *SI Appendix*, Fig. S23 and Table S12), and in particular the IC_{50} of dihydroxylated (**M5**) and glucuronidated metabolites (**G1**) are greater than 100 μM in most of the cell lines tested. These findings can be attributed to higher cellular uptake and lipophilicity (log *P*) (Fig. 3*C*) of **Pt1a** and **M1**–**M4**, while **M5** and **G1** exhibited the lowest cell penetration and log *P*. Additionally, **Pt1a** exhibited time-dependent accumulation in NCI-H460 cancer cells and displayed significantly twofold higher uptake in lung cancer cells compared to that in normal lung fibroblasts (*SI Appendix*, Figs. S24 and S25).

Treatment of NCI-H460 or MDA-MB-231 cells with **Pt1a** (0.5 μM) for 72 h triggered over 70% cancer cell death, mainly at late apoptosis (Fig. 4*A* and *SI Appendix*, Fig. S26), assayed by annexin V-FITC/PI staining. Cell cycle analysis revealed that **Pt1a**-treated cells arrested in the G0/G1 phase (*SI Appendix*, Fig. S27). The luminescence of **Pt1a** was found to be mainly localized in cytoplasm and the mitochondria of NCI-H460 cells with a Pearson's correlation coefficient of 0.77 (*SI Appendix*, Fig. S28) (21). Flow cytometric analysis of the mitochondrial membrane potential ($\Delta\psi_m$) using JC-1 dye revealed that **Pt1a** treatment led to a dramatic reduction in the ratio of red (JC-1 aggregate) to green (JC-1 monomer) fluorescence intensity (*SI Appendix*, Fig. S29), indicating mitochondrial membrane depolarization. **Pt1a** treatment augmented the intracellular oxidant levels as revealed by a 7.6-fold increase in the fluorescence intensity of a 2′,7′-dichlorofluorescein diacetate probe compared with vehicle control (*SI Appendix*, Fig. S30).

In Vitro Antimigratory, Antiinvasive, and Antiangiogenic Properties and Inhibition of Tumorsphere Formation. To determine whether **Pt1a** can inhibit cancer cell motility, a wound-healing scratch assay was performed. As depicted in Fig. 4*B*, compared with vehicle-treated NCI-H460 cells showing almost complete migration into the wound area after 24 h, the migratory ability of **Pt1a**-treated cells was found to be significantly impeded by 79.4%. The antiinvasive property of **Pt1a** was evaluated by Matrigel transwell assay using a highly invasive MDA-MB-231 breast cancer cell line. Compared to the cells exposed to DMSO vehicle (Fig. 4*C*), **Pt1a** treatment reduced the number of MDA-MB-231 cells invading

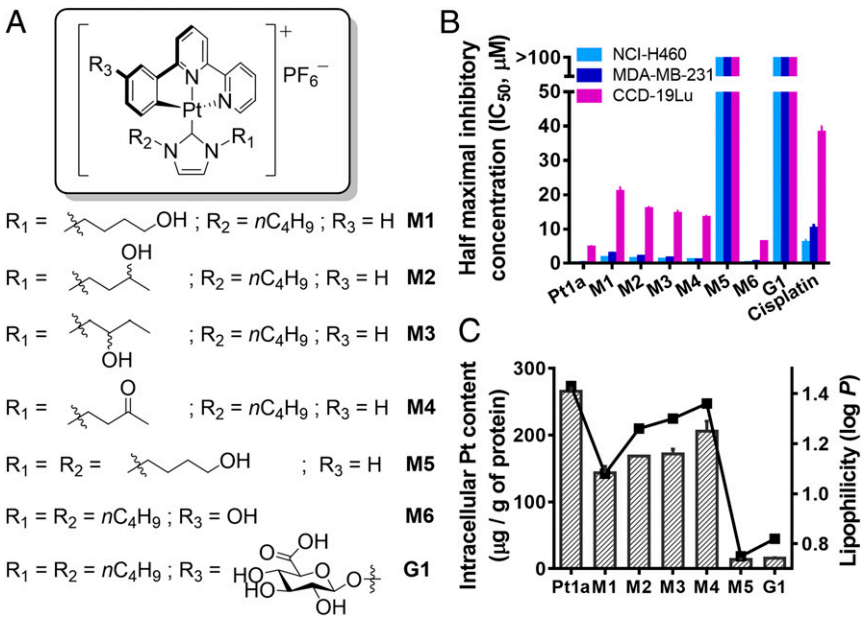

Fig. 3. Metabolite analysis of **Pt1a**. (*A*) Chemical structures of the proposed metabolites (**M1**–**M6** and **G1**) of **Pt1a** identified from microsomal biotransformation reactions and/or renal excretion. (*B*) In vitro cytotoxicity of **Pt1a** and synthesized **M1**–**M6** and **G1** on NCI-H460 lung, MDA-MB-231 breast cancer cells, and CCD-19Lu normal lung fibroblasts. (*C*) Correlation of cellular uptake (hatched bar) in NCI-H460 cells, and lipophilicity (square) of **Pt1a** and different synthetic metabolites.

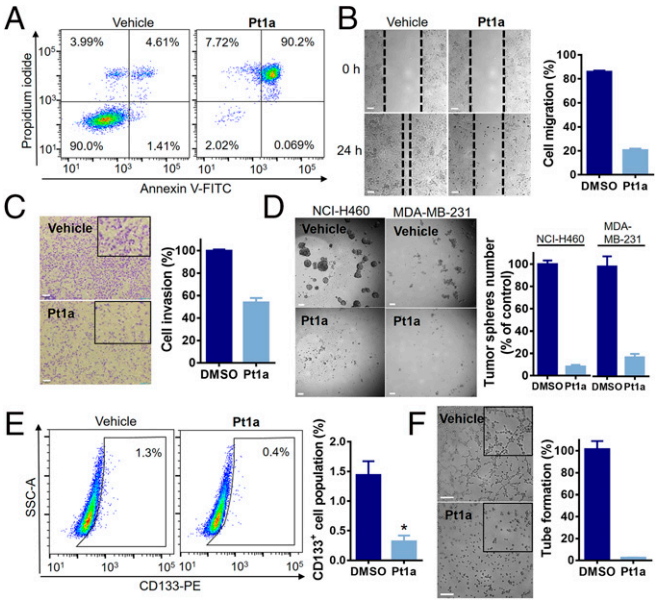

Fig. 4. In vitro anticancer activities of **Pt1a**. (*A*) Flow cytometric analysis of apoptotic cell death of NCI-H460 cells treated with **Pt1a** (0.5 μM) for 72 h. (*B*) Wound-healing assay of NCI-H460 lung cancer cells treated with **Pt1a** (1 μM) for 24 h. (Scale bar, 100 μm.) (*C*) Matrigel invasion assay of MDA-MB-231 breast cancer cells after **Pt1a** treatment (3 μM) for 24 h. (Scale bar, 100 μm.) (*D*) Representative images of secondary (self-renewing) tumor spheres derived from NCI-H460 lung or MDA-MB-231 breast cancer cells after **Pt1a** treatment. (Scale bar, 50 μm.) (*E*) Representative flow cytometry dot plot analysis of CD133 expression of NCI-H460 cells after **Pt1a** treatment (0.1 μM) for 72 h. Data are presented as mean ± SD ($n = 2$; Student's t test, $^*P < 0.05$, compared with DMSO vehicle control). (*F*) Tube-formation assay of MS-1 endothelial cells treated with **Pt1a** (1 μM) for 2 h. (Scale bar, 100 μm.)

through the Matrigel-coated membrane by 46%. Under stem-cell-selective culture conditions, **Pt1a** treatment reduced the number of self-renewed tumor spheres derived from NCI-H460 and MDA-MB-231 cells by 92% and 83%, respectively (Fig. 4*D*). **Pt1a** treatment also reduced the stemness-associated populations of NCI-H460 cells ($CD133^+$) from 1.3% (vehicle) to 0.4% (Fig. 4*E*). In contrast, cisplatin treatment resulted in enrichment of $CD133^+$ NCI-H460 cells (to 16.5%) (*SI Appendix*, Fig. S31). The antiangiogenic activity of **Pt1a** was examined by a tube-formation assay using MS-1 endothelial cells (Fig. 4*F*). In the vehicle control group, MS-1 cells cultured on Matrigel were interconnected to form a branched network. In the presence of **Pt1a** at a subcytotoxic concentration (*SI Appendix*, Fig. S32) the formation of tubular structure was markedly reduced.

In Vivo Tumor Growth Inhibition of Tumor Xenograft and Lung Metastatic Models. The in vivo antitumor efficacy of **Pt1a** was first investigated in comparison with cisplatin using NCI-H460 nonsmall cell lung cancer xenografted nude mouse model. The mice were intravenously administrated with **Pt1a** (3 mg/kg) or cisplatin (1.2 mg/kg) of equivalent platinum dosage. As shown in *SI Appendix*, Fig. S33 *A* and *B*, both **Pt1a** and cisplatin treatment in a 14-d period effectively suppressed tumor growth. However, the body weight of the cisplatin-treated mice kept declining after the third injection at day 4 and its difference from vehicle control was significant at day 14 (*SI Appendix*, Fig. S33*C*). In a biodistribution study, **Pt1a**-treated mice displayed lower accumulation of platinum content in liver, spleen, lung, kidney, and tumor compared to that of cisplatin treatment (*SI Appendix*, Fig. S33*D*). In addition, the in vivo antitumor and antimetastatic activities of **Pt1a** in two independent mouse xenograft and lung metastases models of MDA-MB-231 human breast cancer were studied. The MDA-MB-231 xenograft-bearing mice receiving **Pt1a** (3 mg/kg) by intravenous injection demonstrated an inhibition of tumor growth by 62.5% (Fig. 5*A* and *SI Appendix*, Fig. S34*A*) and a decrease in tumor weight compared with those treated with vehicle (*SI Appendix*, Fig. S34*B*). No apparent difference in body weight of mice was found throughout a 31-d treatment (*SI Appendix*, Fig. S34*C*). Immunohistochemical analysis of the sectioned tumors revealed that **Pt1a** treatment could markedly reduce the expression of VIM compared to vehicle control (Fig. 5*B*); an observation relevant to the tumor differentiation into less invasive epithelial phenotype will be discussed in later sections. For the lung metastases of MDA-MB-231 human breast cancer in nude mouse model, a higher dosage (5 mg/kg) of **Pt1a** was used for the study. As revealed by the bioluminescence images (Fig. 5*C*), **Pt1a** treatment effectively suppressed the growth of metastatic MDA-MB-231 cancer cells in the lung by 80.3% (Fig. 5*D*), with negligible change in body weight in 42 d (Fig. 5*E*). Morphological examination and histological analysis revealed that **Pt1a** treatment significantly reduced the number and area of metastatic nodules in the lungs compared with vehicle control (Fig. 5*F*). Furthermore, no obvious histopathological lesion was observed in heart, liver, spleen, and kidney of **Pt1a**-treated mice (*SI Appendix*, Fig. S35). The weight of the lungs in **Pt1a**-treated mice remained comparable to the normal lungs but smaller in size relative to vehicle control (Fig. 5*G*). Moreover, the in vivo antimetastatic activity of **Pt1a** on B16-F10 melanoma, which is another highly invasive cancer cell line, was investigated. **Pt1a** administration for 14 d attenuated the growth of metastatic B16-F10 melanoma cells in the lung of C57BL/6N mice, as indicated by the reduced number of black nodules in the lungs of mice treated with **Pt1a** compared to vehicle control (Fig. 5 *H* and *I*).

In Vivo Pharmacological Safety Evaluation of Pt1a. Following the in vivo antitumor study of a NCI-H460 xenografted model in the previous part (*SI Appendix*, Fig. S33), blood biochemistry analysis was performed using the blood samples from each group, including vehicle control and **Pt1a**- and cisplatin-treated mice. As revealed by *SI Appendix*, Fig. S36, mice treated with **Pt1a** for 2 wk showed low systemic toxicity with comparable plasma levels of alanine aminotransferase (ALT) and creatinine (CREA) to vehicle control, in which ALT and CREA are liver and kidney damage biomarkers, respectively. However, the renal function of the mice upon cisplatin treatment was found to be impaired, as evidenced by significant elevation of CREA level by 1.65-fold compared to vehicle control. In vivo biosafety studies of **Pt1a** were also evaluated in mouse and rabbit models by a National Medical Products Administration (China)–accredited laboratory. In an acute toxicity study, single-dose intravenous administration of **Pt1a** (20 mg/kg) did not result in mortality, body weight loss, or signs of toxicity in Kunming mice ($n = 20$) after a 14-d observation period (*SI Appendix*, Table S13). No observable abnormality was found in various organ tissues between **Pt1a** and the vehicle control group after necropsy examination. In a mutagenicity test, there was no significant difference in the frequencies of bone marrow micronucleated polychromatic erythrocytes (an indicator of genotoxicity) between mice receiving **Pt1a** (5, 10, and 20 mg/kg) and vehicle control (*SI Appendix*, Table S14). **Pt1a** treatment (0.5 mg/kg) did not show an apparent irritation effect on blood vessels and surrounding tissues of rabbits in a 14-d period (*SI Appendix*, Table S15).

Target Engagement Study of Pt1a. Our previous work using clickable photoaffinity probes has identified six cellular proteins, including VIM, heat-shock protein 60 (HSP60), nucleophosmin (NPM), nuclease-sensitive element binding protein (Y box binding protein, YB-1), nucleoside diphosphate kinase A (NDKA), and peroxiredoxin I (PRDX1), as possible molecular targets of the pincer gold(III)–NHC complex which is isostructural to **Pt1a** (17). Herein,

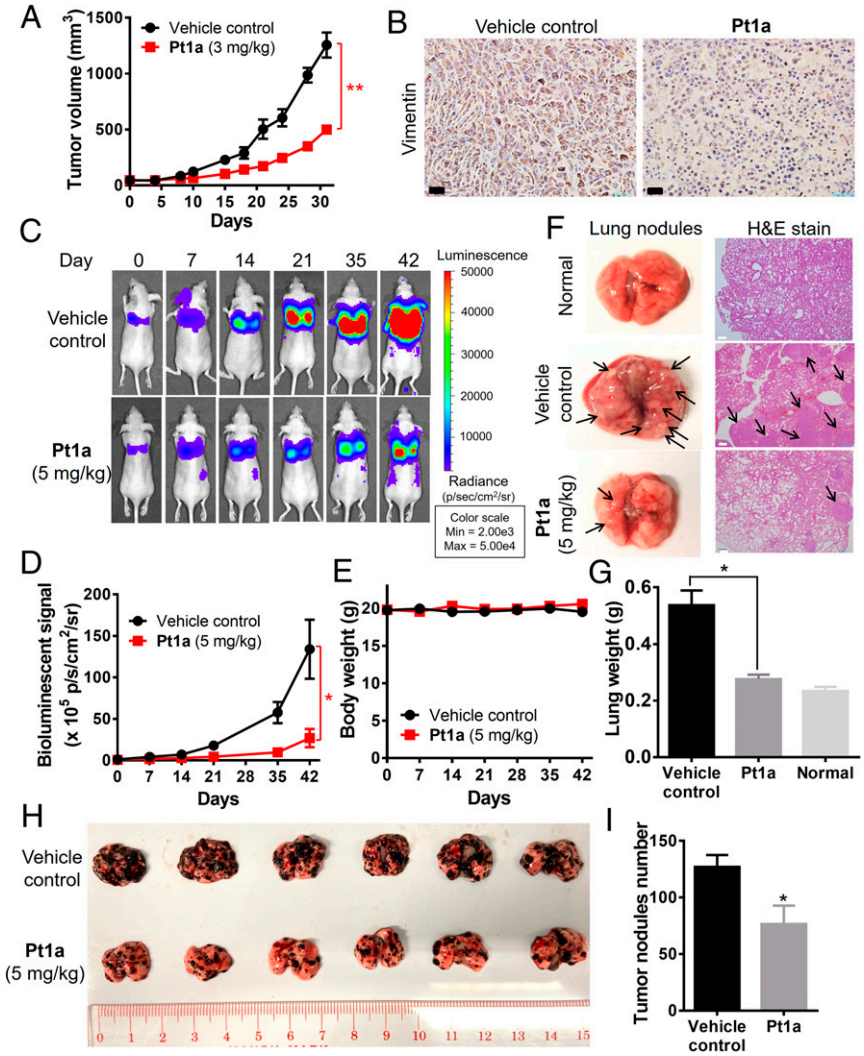

Fig. 5. In vivo antitumor activity of **Pt1a** on tumor xenograft and lung metastatic models. (*A*) Tumor volume of MDA-MB-231 xenografted mice ($n = 4$) after treatment with vehicle or **Pt1a** (3 mg/kg) for 31 d. (*B*) Immunohistochemical analysis of VIM expression in MDA-MB-231 tumor specimens. (Scale bar, 50 μm.) (*C*) Bioluminescence images of mice bearing lung metastases of MDA-MB-231 cells from vehicle and **Pt1a** groups ($n = 6$) throughout a 42-d treatment. (*D*) Normalized bioluminescence signals of lung metastases and (*E*) body weight of mice at different days. (*F*) Representative images and hematoxylin/eosin (H&E) histological staining of the metastases-bearing lungs of mice from vehicle control and **Pt1a** treatment groups at the end point (day 42; arrow: tumor nodules). (Scale bar, 200 μm.) (*G*) The weight of mouse lungs at day 42. (*H*) Photograph of excised lung tissues from mice bearing B16-F10 lung metastases (black nodules) from vehicle and **Pt1a** groups ($n = 6$) throughout a 14-d treatment. (*I*) The numbers of black nodules in excised lungs were counted. Data are presented as mean ± SEM (Student's *t* test, $^*P < 0.05$ and $^{**}P < 0.01$, compared with vehicle control).

we prioritized these putative protein targets in NCI-H460 lung cancer cells upon **Pt1a** treatment using cellular thermal shift assay (CETSA) based on the principle of small-molecule-induced thermal stabilization of target proteins (23). As shown in the immunoblot analysis and thermal stability curves (Fig. 6*A* and *SI Appendix*, Figs. S37 and S38), VIM showed the greatest increase in the melting temperature (T_m) of 3.6 °C by **Pt1a** treatment. Additionally, exposure of cells to **Pt1a** protected the VIM from denaturation at 54 °C in dose-dependent manner as evidenced by a 3.5-fold increase in protein levels compared to untreated control (Fig. 6*B*). The mitochondrial chaperone HSP60 could also be stabilized by **Pt1a**, in which the T_m shift was found to be 1.2 °C in comparison to vehicle control (*SI Appendix*, Fig. S37). The changes in thermal stabilities of the other four protein targets (NPM, YB-1, NDKA, and PRDX1) mediated by **Pt1a** treatment, however, were relatively subtle (*SI Appendix*, Fig. S38).

Disruption of VIM Cytoskeletal Organization. We next investigated the in vitro effects of **Pt1a** on VIM by TEM. Purified VIM protein naturally assembled into filamentous structures in saline solution. In the presence of **Pt1a** at equivalent molar ratio, substantial aggregation occurred (Fig. 6*C*). Immunofluorescence staining experiment of NCI-H460 lung cancer cells demonstrated that, as compared with vehicle control, the VIM network was perturbed by **Pt1a** treatment at a subcytotoxic concentration (3 μM), showing a densely packed aggregation after 8 h (*SI Appendix*, Fig. S39). The obvious contraction of the VIM network from the peripheral leading edge was observed upon prolonged treatment till 24 h (Fig. 6*D*). Importantly, the structural morphology of tubulin-based microtubules remained intact in **Pt1a**-treated cells (Fig. 6*D*), indicative of specific targeting of VIM by **Pt1a**. From the live-cell and time-lapse imaging studies, the intermediate filaments in MDA-MB-231 breast cancer cells expressing mCherry-tagged VIM were shown to reorganize into

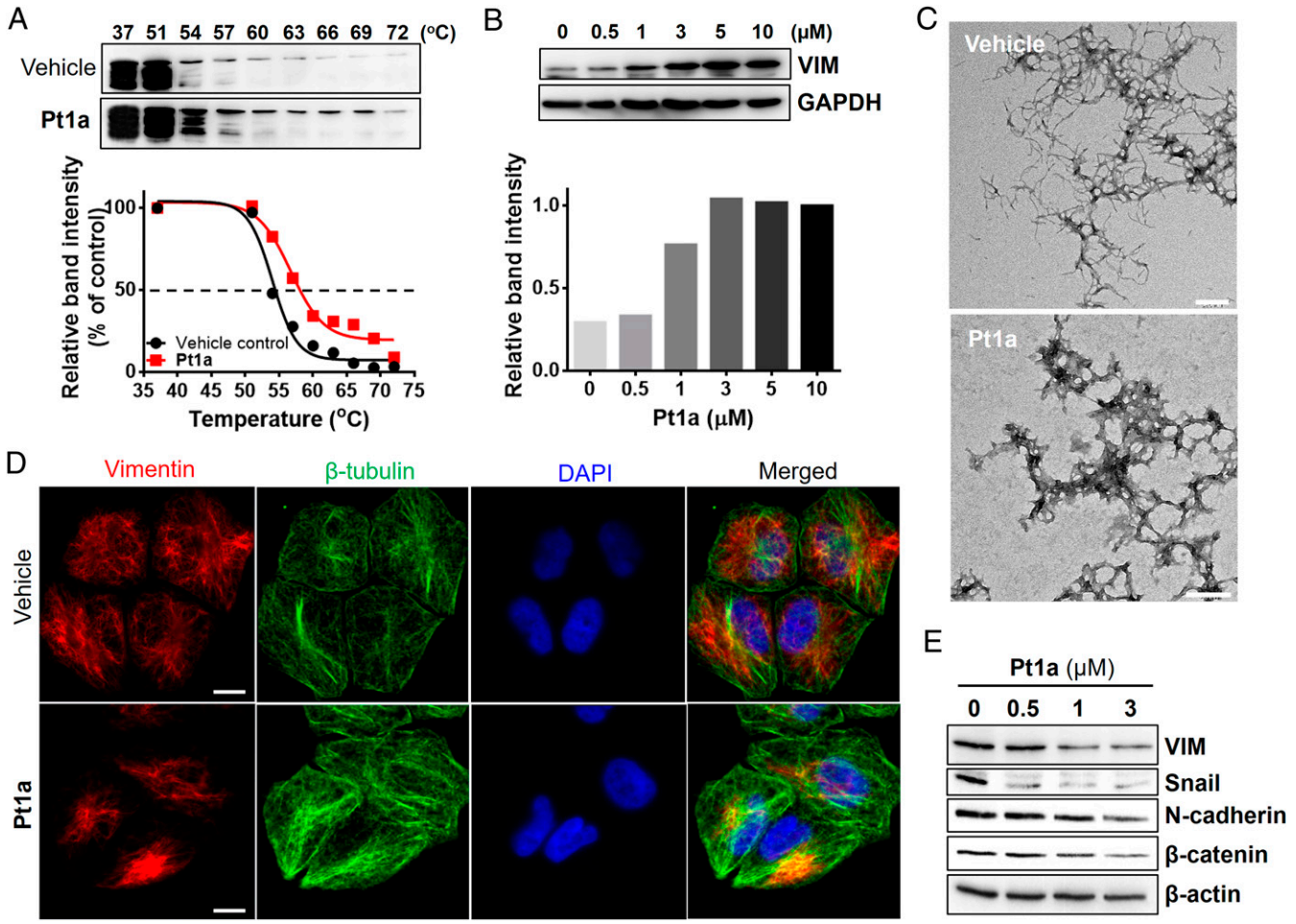

Fig. 6. Engagement of VIM by **Pt1a**. (*A*) Thermal stabilization of VIM following treatment of NCI-H460 cells with **Pt1a** as determined by CETSA. (*B*) Isothermal dose–response stabilization of VIM by **Pt1a** at 54 °C. (*C*) TEM images of the negatively stained VIM intermediate filaments bundle network from the monomeric VIM treated with vehicle or **Pt1a** (3 μM) for 1 h. (Scale bar, 200 nm.) (*D*) Immunofluorescence staining of the VIM filamentous network and tubulin-based microtubules of NCI-H460 cells after treatment with DMSO vehicle or **Pt1a** (3 μM) for 24 h. (The red channel at λ_{ex} = 555 nm and λ_{em} = 560 to 700 nm; the green channel at λ_{ex} = 488 nm and λ_{em} = 510 to 530 nm; the blue channel at λ_{ex} = 405 nm and λ_{em} = 430 to 470 nm). The merged image of red, green, and blue channels is also shown. (Scale bar, 10 μm.) (*E*) Expression of mesenchymal protein markers in NCI-H460 cells after dose-dependent treatment of **Pt1a** for 24 h.

perinuclear bundles in response to **Pt1a** treatment over 8 h (*SI Appendix*, Fig. S40). The green luminescence of **Pt1a** was also found to partially colocalized with the red fluorescence of the VIM network (Pearson's correlation coefficient of 0.61; *SI Appendix*, Fig. S41). The expression of VIM and other EMT-associated proteins was investigated by immunoblot analysis. Upon treatment of cells with **Pt1a** for 24 h, the expression of mesenchymal markers, including VIM, Snail, N-cadherin, and β-catenin, whose functions are linked to cancer cell migration and invasion (3, 24), were down-regulated (Fig. 6*E*).

Binding Interactions with VIM. The binding interactions between purified VIM protein and **Pt1a** were first studied using NMR spectroscopy. In the presence of VIM, the proton peaks of **Pt1a** display broadening accompanied by reduced intensity in the ^{1}H NMR spectrum (Fig. 7*A*). The biomolecular binding was further supported by saturation transfer difference (STD) NMR experiments based on saturation of the magnetization of receptor protein being transferred to a bound ligand (25). The STD intensity for the protons of **Pt1a** was shown to be significantly enhanced in the presence of VIM relative to the negligible STD response for **Pt1a** alone. By determining the binding epitopes of **Pt1a** to VIM with normalized STD amplification factor as a function of saturation time (Fig. 7*B* and *SI Appendix*, Fig. S42), the aromatic protons signals (H2–H6) of the pincer C^N^N moiety as well as the proton pairs of H12 and H16 on NHC ligand exhibited a relatively pronounced STD effect, implying that those ligand atoms are in close proximity to the binding site of VIM. Surface plasmon resonance (SPR) measurements revealed a dose-dependent increase in the binding responses of **Pt1a** to the immobilized VIM (Fig. 7*C*), reaching saturable steady-state binding with an equilibrium dissociation constant (K_D) of 1.06 μM. **Pt1b** having shortened *N*-alkyl chains bearing two *N*-methyl groups displayed about 1.8-fold reduction in binding affinity (K_D: 1.86 μM). **Pt4** having thiophene instead of phenyl ring in pincer C^N^N moiety (K_D: 1.95 μM) and **Pt6** consisting of benzimidazole-derived NHC (K_D: 2.11 μM) showed a modest decrease in binding affinity compared to **Pt1a** (Fig. 7*D* and *SI Appendix*, Fig. S43). Fluorescence titration experiment of VIM with increasing concentrations (0.5 to 9 μM) of **Pt1a** revealed a dose-dependent decrease in the fluorescence of tryptophan and tyrosine residues (*SI Appendix*, Fig. S44) and a binding constant was estimated in low micromolar concentration (K_D: 1.25 μM; tryptophan). Time-resolved lifetime measurement revealed a

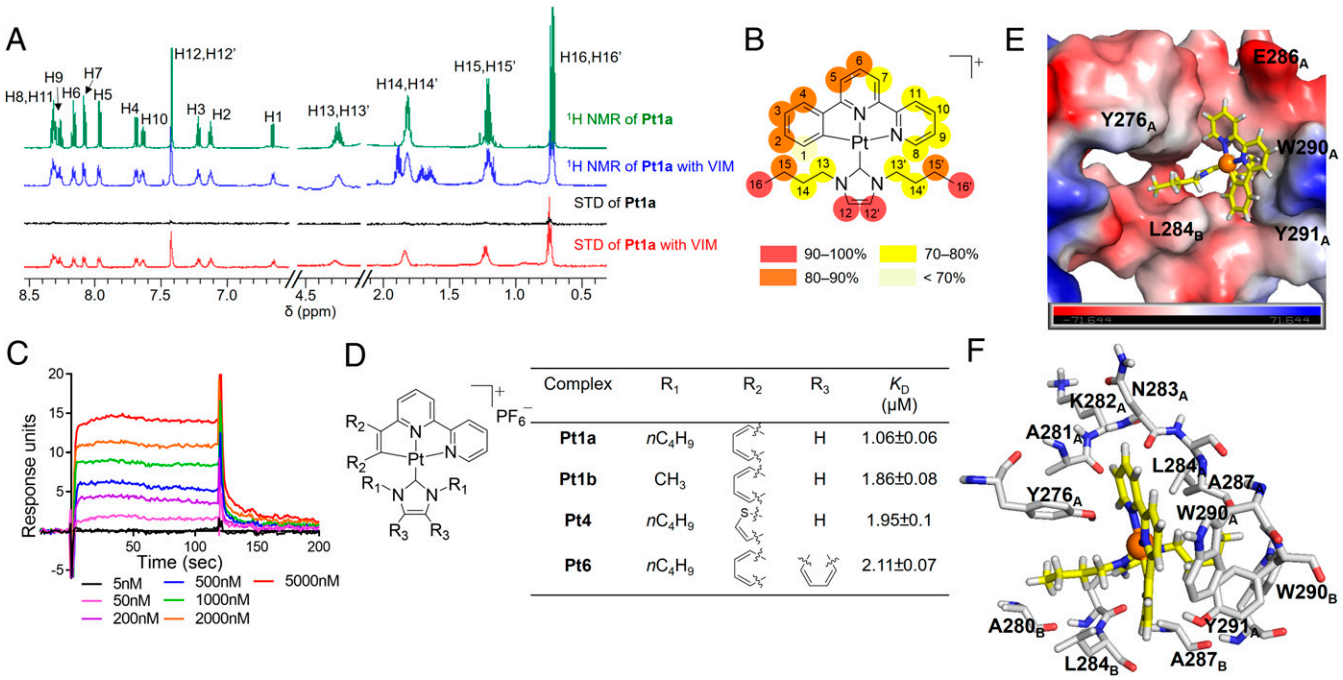

Complex	R_1	R_2	R_3	K_D (μM)
Pt1a	nC_4H_9		H	1.06±0.06
Pt1b	CH_3		H	1.86±0.08
Pt4	nC_4H_9		H	1.95±0.1
Pt6	nC_4H_9			2.11±0.07

Fig. 7. Molecular binding studies of **Pt1a** with VIM. (*A*) ^{1}H and STD NMR spectra of **Pt1a** (100 μM) or **Pt1a** with VIM at a ligand:protein ratio of 10:1. (*B*) Proposed binding epitope mapping of **Pt1a** with normalized STD intensities. Deep red circles indicate the most intense STD effect. (*C*) Representative SPR sensorgrams for the binding interaction of **Pt1a** (5 to 2,000 nM) to immobilized VIM. (*D*) Binding affinity constants of Pt(II) complexes to VIM as determined by SPR analysis. Data are presented as mean ± SD; $n = 2$. (*E*) MD simulation of the binding interaction between **Pt1a** and a VIM dimer. The electrostatic potential surface of the binding pocket at the middle of the coil 2A domain is shown with red as negative and blue as positive. The hydrogen, carbon, nitrogen, and Pt atoms of **Pt1a** are colored in white, yellow, blue, and orange, respectively. Critical residues are labeled with the chain identity in A or B in the dimer as subscript letters. (*F*) Interactions of **Pt1a** with surrounding amino acid residues in the pocket are shown in stick model. Carbon and oxygen atoms are colored in light gray and red, respectively, whereas the rest are the same as in *E*. *E* and *F* were prepared using PyMOL (Schrödinger, LLC.).

decrease in fluorescence lifetime (τ) of the tryptophan residue of VIM from 3.02 (in the absence of **Pt1a**) to 2.62 ns in the 1:2 VIM–**Pt1a** ratio with biexponential decay (*SI Appendix*, Fig. S45 *A* and *B*). On the basis of the spectral overlap between emission spectrum of tryptophan residue (donor) and absorption spectrum of **Pt1a** (acceptor) (*SI Appendix*, Fig. S46), the distance between **Pt1a** and tryptophan residue of VIM is estimated based on Förster resonance energy transfer (FRET) theory (26) to be 15.9 Å. Emission titration using VIM as the titrant revealed a binding constant K_D of 7.7 μM, estimated based on enhancement of emission of **Pt1a** at λ_{em} = 490–770 nm upon increasing concentrations (1 to 5 μM) of VIM (*SI Appendix*, Fig. S47). Addition of VIM also resulted in increased excited state lifetime of **Pt1a** from 0.49 μs (free **Pt1a**) to 0.99 μs (**Pt1a**+VIM) (*SI Appendix*, Fig. S48). This may be attributed to restricted molecular motion of and less accessibility to platinum–substrate interaction in the excited state of **Pt1a** upon VIM binding, as similarly reported in other luminescent platinum(II) complexes upon intercalation to nucleic acids and binding to proteins (27, 28).

Molecular Dynamics Simulations. By employing cosolvent molecular dynamics (MD) simulations on the currently longest dimeric structural model (residues S144 to K334) of VIM rod (29), a possible binding pocket in VIM for **Pt1a** was identified to be centered around L284 of chain B and flapped by aromatic residues (Y276, W290, and Y291 of chain A) (Fig. 7*E*). The fragment (residues A247 to K334, denoted as L12C2A) spanning over the binding pocket was extracted for molecular docking and the predicted complex of L12C2A and **Pt1a** was subjected to MD simulations. In the simulated model, the NHC moiety is sandwiched between the helices and the *N*-butyl chains are surrounded by hydrophobic residues. One butyl group of the NHC extends between Y276 of chain A and A280 and L284 of chain B, while another butyl chain forms close contacts with the aromatic side chains of Y291 of chain A and W290 of chain B (Fig. 7*F*). For the pincer $[Pt^{II}(C\hat{}N\hat{}N)]^+$ motif, the phenyl group and the central pyridine are located in a more nonpolar environment. The phenyl moiety is close to Y291 of chain A and the central pyridine attaches tightly to the indole side chain of W290 (chain A) with distances in the range of 6.65 to 7.60 Å (*SI Appendix*, Fig. S49). In contrast, the peripheral pyridine ring of the C^N^N ligand is oriented toward the backbone residues of K282 and N283 with polar side chains. These interactions are consistent with our NMR data which show that the terminal methyl groups and the imidazole ring of the NHC ligand experience more significant saturation transfer upon binding. The binding affinity K_D based on this simulated model is estimated to be 4.56 μM, which is comparable to the SPR result (1.06 μM).

Discussion

Examples of anticancer transition metal complexes showing in vivo antimetastatic activity are sparse in the literature. For the clinically used platinum-based anticancer drugs, their antimetastatic efficacy is only rarely active unless they are combined with other anticancer drugs (30, 31). Herein, the pincer $[Pt^{II}(C\hat{}N\hat{}N)(NHC)]^+$ complexes display a broad spectrum of anticancer activities, in which **Pt1a** shows both effective cytotoxic effect and in vivo antimetastatic activity with favorable pharmacological safety. The self-assembly of pincer $[Pt^{II}(C\hat{}N\hat{}N)(NHC)]^+$ complexes to form nanoparticles in aqueous solution and culture medium (Fig. 2 *B* and *C* and *SI Appendix*, Fig. S6*B*) is an appealing feature for much more Pt accumulation in cancer cells compared to normal fibroblasts (*SI Appendix*, Fig. S25) through endocytosis (32), which may

result in preferential cytotoxicity of this class of complexes to cancer cells over normal cells (Table 1 and *SI Appendix*, Fig. S7).

VIM is a key cytoskeletal component in mesenchymal cancer cells, which are often endowed with tumor-initiating and metastatic properties. Increased VIM expression is identified in various tumor types and correlated with cancer aggressiveness and poor clinical outcome (3, 5). Thus, VIM-targeting compounds are advantageous for development of effective chemotherapeutic agents via inhibiting the cancer stemness and metastasis. Here, the engagement of **Pt1a** with VIM was evidenced by the following experiments: 1) CETSA (Fig. 6 *A* and *B*), 2) ^{1}H, ^{1}H STD NMR and epitope mapping (Fig. 7 *A* and *B*), 3) SPR (Fig. 7 *C* and *D*), and 4) MD simulations (Fig. 7 *E* and *F*). The binding interactions between **Pt1a** and VIM are distinct from those previously reported VIM-targeting organic compounds. In the literature, compounds bearing reactive electrophiles (e.g., Michael acceptor) such as withaferin A and 4-hydroxynonenal were found to covalently bind to VIM on Cys328 residue at the N terminus of the coil 2B domain (11, 13). A fluorescent chemical probe TiY (33) that selectively stains tumor-initiating cells was shown to bind VIM via the same binding site (11). Arylquin 1 targeted VIM to induce secretion of prostate-apoptosis-response-4 and was demonstrated through computational modeling to bind to a hydrophobic pocket between a pair of head-to-tail α-helical dimers in the tetrameric VIM (12). Herein, a model of biomolecular interaction between **Pt1a** and VIM was established using epitope mapping by STD NMR analysis and MD simulations. The orthogonal scaffold of **Pt1a** composed of cyclometalated pincer [Pt^{II}(C^N^N)] plane and NHC moiety with the *N*-butyl chains displays hydrophobic contacts with the proximal amino acid residues (e.g., tryptophan and tyrosine) at the middle of the coil 2A domain of VIM dimer (Fig. 7 *E* and *F*), resulting in geometrical distortion of the extended rod. In addition to the SPR binding analysis (Fig. 7 *C* and *D*), the binding interaction between **Pt1a** and VIM has also been revealed by fluorescence quenching of the aromatic tryptophan residue (W290) of VIM in the presence of **Pt1a** (*SI Appendix*, Fig. S44) as well as enhancement of emission intensity and increase in emission lifetime of **Pt1a** in the presence of VIM (*SI Appendix*, Figs. S47 and S48). While there is variation in the binding constants (K_D) estimated from different experiments, all these values are in the low micromolar regime. The observed quenching of W290 fluorescence by **Pt1a** can be ascribed to fluorescence energy transfer from W290 to **Pt1a**. The intermolecular distance between W290 of VIM (donor) and **Pt1a** (acceptor) calculated from FRET analysis is 15.9 Å (*SI Appendix*, Fig. S46*B*), being comparable (within a factor of 2) to that of 7.60 to 8.22 Å obtained by MD simulations based on the complex formed between **Pt1a** and full-rod dimeric VIM model (*SI Appendix*, Fig. S49). Such intermolecular distance together with the spectral overlap of fluorescence spectrum of W290 and absorption spectrum of **Pt1a** (*SI Appendix*, Fig. S46*A*) are supportive of fluorescence energy transfer in quenching of W290 fluorescence by **Pt1a**. The coil 2A domain was recently reported to be more dynamic than the N-terminal coil 1A and coil 1B domains for the proper cross-coiling mechanism (34). The MD simulations on the complex formed between **Pt1a** and the dimeric model of VIM rod (residues S144 to K334) further reveal that the binding of **Pt1a** to the coil 2A domain of VIM dimer distorts the geometry of the extended rod (*SI Appendix*, Fig. S50). It is envisaged that such structural distortion upon **Pt1a** binding can result in perturbation of the regular assembly of the VIM intermediate filament.

The structural scaffold of the pincer Pt(II)–NHC system should be amenable to modifications on both pincer C^N^N and NHC ligands for tuning the anticancer activities. Comparable antiproliferative activity toward different cancer cell lines (Table 1 and *SI Appendix*, Fig. S7) and a modest decrease in the VIM binding affinity were observed when **Pt1a** was modified to contain thiophene-substituted C^N^N (**Pt4**) or benzimidazole-derived NHC ligands (**Pt6**) (Fig. 7*D*). Importantly, increasing the *N*-alkyl chain length (butyl for **Pt1a** versus methyl for **Pt1b**) consistently enhances the cell growth inhibition toward all cancer cell lines examined. This also resulted in slightly higher VIM binding affinity, attributable to a modulation on the nonpolar interactions between *N*-alkyl groups with the proximal amino acid residues (Fig. 7 *E* and *F*).

In line with the biological consequences of targeting VIM, we have been able to show that **Pt1a** exhibited in vitro antimigratory and antimetastatic activities (Fig. 4 *B* and *C*). **Pt1a** induced the aggregation of VIM filaments in vitro (Fig. 6*C*) and collapse of the VIM networks in cells, whereas tubulin-based microtubules remained unaffected (Fig. 6*D*). **Pt1a** treatment was also shown to reduce the expression of VIM and other mesenchymal proteins involved in tumorigenesis and metastasis, including N-cadherin and β-catenin, which form protein complexes mediating transendothelial migration (35), and Snail, which is the transcriptional factor controlling expression of proteins involved in EMT (Fig. 6*E*) (24). In addition, **Pt1a** inhibited the self-renewal growth of tumorspheres (Fig. 4*D*) derived from cancer stem cells which were shown to highly express VIM as a biomarker (3, 33). **Pt1a** treatments were demonstrated to display promising in vivo antitumor and antimetastatic activities against NCI-H460, MDA-MB-231, and B16-F10 cancers with high expression of VIM (Fig. 5 and *SI Appendix*, Figs. S33 and S34). The reduced VIM immunostaining in the shrunken tumors of **Pt1a**-treated xenografted mice (Fig. 5*B*) are presumably related to the specificity of VIM engagement by **Pt1a**.

Despite the ubiquitous use of cisplatin in chemotherapy, dose-limiting toxicities are frequently encountered (36). In this work, **Pt1a** could be administrated without significant adverse effects in animals. Mice having lung metastasis of human breast cancer MDA-MB-231 could tolerate 42 d of multiple administration of **Pt1a** treatment (5 mg/kg), displaying no body weight loss or organ damage (Fig. 5*E* and *SI Appendix*, Fig. S35). Importantly, there is a large safety window of **Pt1a** as indicated by 14-d acute toxicity study showing no lethality at maximally tested dosage of 20 mg/kg (*SI Appendix*, Table S13). The in vivo tolerability of **Pt1a** could be attributable to the generation of oxidized and glucuronidated metabolites, involving the hydroxylation of the *N*-butyl chain of the coordinated NHC ligand and glucuronide conjugation to corresponding hydroxylated species (Fig. 3 and *SI Appendix*, Fig. S22) that are renal-clearable (*SI Appendix*, Fig. S15) and display reduced in vitro potency on cell growth inhibition (*SI Appendix*, Table S12 and Fig. S23).

Conclusions

In summary, we have identified **Pt1a** as a highly effective antitumor compound targeting to VIM with high binding affinity with a K_D of 1 μM and which has been shown to be effective in suppressing tumor initiation and metastasis. Noncovalent binding interactions of **Pt1a** with VIM involving the [Pt^{II}(C^N^N)] plane and NHC motif arranged in an orthogonal scaffold is essential for the molecular targeting. The scaffold of **Pt1a** also allows the complex to be biotransformed into less toxic and renal-clearable metabolites. Our studies highlight the pincer-type platinum(II)–NHC complexes to be developed as a new generation of platinum-targeted chemotherapy for combating metastatic cancers.

Materials and Methods

Details of the materials, experimental procedures, and data, including synthesis and characterization, photophysical measurement, X-ray crystallography, self-assembly studies, metabolite analysis, cellular thermal shift assay, biomolecular binding (STD–NMR protein binding, SPR, and emission titration experiments), MD simulations, in vitro anticancer, and in vivo antitumor studies are described in *SI Appendix*.

Data Availability. X-ray crystallographic data have been deposited in The Cambridge Crystallographic Data Centre, https://www.ccdc.cam.ac.uk/ (accession nos. 2008384, 2008385, and 2008386). All study data are included in the article and/or *SI Appendix*.

ACKNOWLEDGMENTS. We acknowledge the Innovation and Technology Fund (ITS/488/18) and funding support from the Laboratory for Synthetic Chemistry and Chemical Biology under the Health@InnoHK Program launched by the Innovation and Technology Commission. We thank Mr. Frankie Chan for TEM analysis. We thank The University of Hong Kong Li Ka Shing Faculty of Medicine Centre for PanorOmic Sciences Imaging and Flow Cytometry Core and the Department of Physics of the City University of Hong Kong for instrumental support.

1. C. L. Chaffer, R. A. Weinberg, A perspective on cancer cell metastasis. *Science* **331**, 1559–1564 (2011).
2. J. P. Thiery, Epithelial-mesenchymal transitions in tumour progression. *Nat. Rev. Cancer* **2**, 442–454 (2002).
3. S. A. Mani *et al*., The epithelial-mesenchymal transition generates cells with properties of stem cells. *Cell* **133**, 704–715 (2008).
4. T. Shibue, R. A. Weinberg, EMT, CSCs, and drug resistance: The mechanistic link and clinical implications. *Nat. Rev. Clin. Oncol.* **14**, 611–629 (2017).
5. A. Satelli, S. Li, Vimentin in cancer and its potential as a molecular target for cancer therapy. *Cell. Mol. Life Sci.* **68**, 3033–3046 (2011).
6. S. Grünert, M. Jechlinger, H. Beug, Diverse cellular and molecular mechanisms contribute to epithelial plasticity and metastasis. *Nat. Rev. Mol. Cell Biol.* **4**, 657–665 (2003).
7. B. Sun *et al*., Identification of metastasis-related proteins and their clinical relevance to triple-negative human breast cancer. *Clin. Cancer Res.* **14**, 7050–7059 (2008).
8. N. Yamashita *et al*., Significance of the vimentin expression in triple-negative breast cancer. *J. Clin. Oncol.* **31**, 1056 (2013).
9. A. M. Richardson *et al*., Vimentin is required for lung adenocarcinoma metastasis via heterotypic tumor cell-cancer-associated fibroblast interactions during collective invasion. *Clin. Cancer Res.* **24**, 420–432 (2018).
10. K. Pang *et al*., RNF208, an estrogen-inducible E3 ligase, targets soluble Vimentin to suppress metastasis in triple-negative breast cancers. *Nat. Commun.* **10**, 5805 (2019).
11. P. Bargagna-Mohan *et al*., The tumor inhibitor and antiangiogenic agent withaferin A targets the intermediate filament protein vimentin. *Chem. Biol.* **14**, 623–634 (2007).
12. R. Burikhanov *et al*., Arylquins target vimentin to trigger Par-4 secretion for tumor cell apoptosis. *Nat. Chem. Biol.* **10**, 924–926 (2014).
13. D. Pérez-Sala *et al*., Vimentin filament organization and stress sensing depend on its single cysteine residue and zinc binding. *Nat. Commun.* **6**, 7287 (2015).
14. M. J. Bollong *et al*., A vimentin binding small molecule leads to mitotic disruption in mesenchymal cancers. *Proc. Natl. Acad. Sci. U.S.A.* **114**, E9903–E9912 (2017).
15. M. Dörr, E. Meggers, Metal complexes as structural templates for targeting proteins. *Curr. Opin. Chem. Biol.* **19**, 76–81 (2014).
16. D. Hu *et al*., Anticancer gold(III) porphyrins target mitochondrial chaperone Hsp60. *Angew. Chem. Int. Ed. Engl.* **55**, 1387–1391 (2016).
17. S.-K. Fung *et al*., Cyclometalated gold(III) complexes containing N-heterocyclic carbene ligands engage multiple anti-cancer molecular targets. *Angew. Chem. Int. Ed. Engl.* **56**, 3892–3896 (2017).
18. T. Zou *et al*., Anticancer metal-N-heterocyclic carbene complexes of gold, platinum and palladium. *Curr. Opin. Chem. Biol.* **43**, 30–36 (2018).
19. S. Jurgens, F. E. Kuhn, A. Casini, Cyclometalated complexes of platinum and gold with biological properties: State-of-the-art and future perspectives. *Curr. Med. Chem.* **25**, 437–461 (2018).
20. S. M. Meier-Menches *et al*., An organometallic gold(I) bis-N-heterocyclic carbene complex with multimodal activity in ovarian cancer cells. *Chemistry* **26**, 15528–15537 (2020).
21. R. W. Sun *et al*., Luminescent cyclometalated platinum(II) complexes containing N-heterocyclic carbene ligands with potent in vitro and in vivo anti-cancer properties accumulate in cytoplasmic structures of cancer cells. *Chem. Sci. (Camb.)* **2**, 728–736 (2011).
22. K. Li, T. Zou, Y. Chen, X. Guan, C.-M. Che, Pincer-type platinum(II) complexes containing N-heterocyclic carbene (NHC) ligand: Structures, photophysical and anion-binding properties, and anticancer activities. *Chemistry* **21**, 7441–7453 (2015).
23. D. Martinez Molina *et al*., Monitoring drug target engagement in cells and tissues using the cellular thermal shift assay. *Science* **341**, 84–87 (2013).
24. K. Ito, S. H. Park, A. Nayak, J. H. Byerly, H. Y. Irie, PTK6 inhibition suppresses metastases of triple-negative breast cancer via SNAIL-dependent E-cadherin regulation. *Cancer Res.* **76**, 4406–4417 (2016).
25. M. Mayer, B. Meyer, Characterization of ligand binding by saturation transfer difference NMR spectroscopy. *Angew. Chem. Int. Ed. Engl.* **38**, 1784–1788 (1999).
26. T. Förster, Zwischenmolekulare Energiewanderung und Fluoreszenz. *Ann. Phys.* **437**, 55–75 (1948).
27. S.-K. Fung *et al*., Luminescent platinum(II) complexes with functionalized N-heterocyclic carbene or diphosphine selectively probe mismatched and abasic DNA. *Nat. Commun.* **7**, 10655 (2016).
28. A. S. Law, L. C. Lee, M. C. Yeung, K. K. Lo, V. W. Yam, Amyloid protein-induced supramolecular self-assembly of water-soluble platinum(II) complexes: A luminescence assay for amyloid fibrillation detection and inhibitor screening. *J. Am. Chem. Soc.* **141**, 18570–18577 (2019).
29. D. D. Gae *et al*., Completion of the vimentin rod domain structure using experimental restraints: A new tool for exploring intermediate filament assembly and mutations. *Structure* **27**, 1547–1560.e4 (2019).
30. A. Bergamo, G. Sava, Linking the future of anticancer metal-complexes to the therapy of tumour metastases. *Chem. Soc. Rev.* **44**, 8818–8835 (2015).
31. J. Balmaña *et al*., Phase I trial of olaparib in combination with cisplatin for the treatment of patients with advanced breast, ovarian and other solid tumors. *Ann. Oncol.* **25**, 1656–1663 (2014).
32. S. Behzadi *et al*., Cellular uptake of nanoparticles: Journey inside the cell. *Chem. Soc. Rev.* **46**, 4218–4244 (2017).
33. Y. A. Lee *et al*., Identification of tumor initiating cells with a small-molecule fluorescent probe by using vimentin as a biomarker. *Angew. Chem. Int. Ed. Engl.* **57**, 2851–2854 (2018).
34. A. Premchandar *et al*., Structural dynamics of the vimentin coiled-coil contact regions involved in filament assembly as revealed by hydrogen-deuterium exchange. *J. Biol. Chem.* **291**, 24931–24950 (2016).
35. G. Li, K. Satyamoorthy, M. Herlyn, N-cadherin-mediated intercellular interactions promote survival and migration of melanoma cells. *Cancer Res.* **61**, 3819–3825 (2001).
36. L. Kelland, The resurgence of platinum-based cancer chemotherapy. *Nat. Rev. Cancer* **7**, 573–584 (2007).